# Unlocking the Electrochemical-Mechanical Coupling Behaviors of Dendrite Growth and Crack Propagation in All-Solid-State Batteries

Chunhao Yuan[1,2], Wenquan Lu[3], Jun Xu[1,2*]

[1]*Department of Mechanical Engineering and Engineering Science, The University of North Carolina at Charlotte, Charlotte, NC 28223, USA*

[2]*Vehicle Energy & Safety Laboratory (VESL), North Carolina Motorsports and Automotive Research Center, The University of North Carolina at Charlotte, Charlotte, NC 28223, USA*

[3]*Chemical Sciences and Engineering Division, Argonne National Laboratory, Lemont, IL 60439, USA*

[*]Corresponding author: Prof. Jun Xu, Email: jun.xu@uncc.edu

**Abstract**: Dendrite growth and crack propagation are two major hurdles on the road towards the large-scale commercialization of lithium metal all-solid-state batteries (ASSBs). Due to the highly multiphysics coupled nature of the underlying dendrite growth mechanism, its understanding has been difficult and limited. Herein, for the first time, we establish an electrochemical-mechanical model directly coupling dendrite growth and crack propagation from a physics-based perspective at the cell level. Results reveal that overpotential-driven stress propels a crack to penetrate through the solid electrolyte, creating vacancies for dendrite growth, leading to the short circuit of the battery. Thus, the high lithiation/charging rate and low conductivity of electrolytes can accelerate the electrochemical failure of the battery. We further discover that Young's modulus $E_{LLZO}$ of the electrolyte has competing contributions to the fracture and dendrite growth; specifically, when $E_{LLZO}$ =40~100 GPa, the short circuit will be triggered early. A larger toughness value hinders the crack propagation and mitigates the Li dendrite growth. The developed multiphysics model provides an in-depth understanding of the coupling of crack propagation and dendrite growth within ASSBs and an insightful mechanistic design guidance map for robust and safe ASSB cells.

Keywords: All-solid-state battery, Dendrite growth, Crack propagation, Short circuit, Electrochemical-mechanical model

## 1 Introduction

The wide spread of lithium-ion batteries has witnessed considerable safety issues caused by various abusive loadings,[1] creating an urgent demand for next-generation batteries with high safety performance and high energy density.[2] Compared with conventional organic and flammable liquid electrolytes, solid electrolytes (SEs) possess a nonflammable nature and the ability to improve battery energy density significantly.[3] As such, all-solid-state batteries (ASSBs) are regarded as one of the most promising candidates to satisfy the increasingly stringent safety- and energy-density requirements.[4] Although the ion conductivity of SEs has greatly improved to be comparable to the liquid electrolytes,[5] lithium dendrite growth and crack propagation in SEs remain two major safety issues. The corresponding short-circuit failures and poor cyclability problems are the two main obstacles that hinder the wide commercialization of ASSBs.[4, 6]

Lithium dendrites and cracks in SEs are reported to initiate at the lithium electrode/SE interface,[7] mainly within the initial defects, such as open pores, voids, cracks, and grain boundaries.[6d, 8] Above the critical current density, the driving force is strong enough for Li dendrite growth to oppose the mechanical resistive force.[6d] Generally, the dendrite growth drives cracks to propagate within SEs, and the newly formed crack provides the vacant space for dendrites to grow further.[7b] Such synergic evolution behavior eventually causes a short circuit of the battery.[7b, 9]

Plenty of pioneering efforts from the perspective of material science have addressed the dendritic and interfacial issues, mainly with respect to three aspects, i.e., 1) advanced

structure design of the electrode or current collector to accommodate the newly grown Li dendrite and release the stress;[10] 2) interfacial modification to improve the solid-solid contact property between the electrode and SE;[11] and 3) improvement of SE electrochemical/mechanical properties to suppress dendrite growth and improve battery performance.[12] From the mechanical perspective, stacking pressure is found to significantly influence dendrite growth, crack propagation, and interface stability[8b, 13] such that the concept of applying residual compressive stress in SEs is introduced to prevent dendrite penetration.[14] Although the performance of ASSBs has been greatly enhanced, inevitable dendrite growth still occurs during charging/discharging,[9] and the critical current density and cyclability performance need to be improved as well.[11c, 15]

An experimental investigation is regarded as the most straightforward methodology to understand the underlying mechanism of dendritic and interfacial issues. Various *in-situ* and *ex-situ* experimental characterizations have discovered that the interfacial defect initiated dendrite growth and crack propagation.[16] *In-situ* scanning electron microscopy (SEM) observed that the deposited Li grows along the grain boundaries and causes cracks in a $Li_2S$-$P_2S_2$ SE.[17] In a polycrystalline $Li_{6.25}Al_{0.25}La_3Zr_2O_{12}$ SE, Li dendrite preferentially grows in the grain boundaries.[18] With the aid of focused ion beam (FIB)-SEM, it was discovered that the interfacial contact loss caused by cathode volume expansion resulted in battery capacity fade during cycling,[6c] providing a possible reason for the poor cyclability of ASSBs. By using *operando* optical microscopy, multiple dendrite morphologies were revealed to penetrate the $Li_7La_3Zr_2O_{12}$(LLZO) SE, i.e., straight,

branching, spalling, and diffuse modes.[9] With the help of an atomic force microscope (AFM), Li whisker growth-induced mechanical stress under specific applied voltage was quantitatively measured.[19] Interestingly, Li dendrites were also observed to grow only along the crack area, using X-ray computed tomography (CT).[7b]

The above state-of-the-art experimental results directly demonstrate the phenomena of Li dendrite growth and crack propagation within SEs, and thus provide an initial understanding of the coupling behaviors. However, more theoretical understanding of the mechanisms requires rigorous physics-based modeling work. Dendrite initiation and growth rate in ceramic SEs were theoretically explored by bridging the dendrite growth with the electrochemical potential.[20] The electrochemical-mechanical model studied the effect of bending of SE on cell potential and lithiation capacity.[21] The coupled phase-field model showed that excess surface electrons significantly affect the initiation positions of Li dendrites within the grain boundaries of polycrystalline LLZO SE.[8a, 22] By direct numerical simulation of restructured SE microstructure, the effective SE properties were obtained, and the effects of operating conditions, including temperature and external pressure, were parametrically studied.[23] The stack pressure and SE electrochemical properties were found able to influence the interfacial deposition and mechanical stability.[13a] The interaction mechanism of crack propagation and dendrite growth under stacking pressures and the interfacial defect was further explored by the one-way coupled electrochemical-mechanical phase-field model.[8b] These numerical models provide an in-depth understanding of the dendritic and interfacial issues, mainly at the grain level.

However, currently available modeling work is not built in a fully electrochemical-mechanical coupled fashion, and, moreover, the model cannot describe the cell-level behavior, and thus is incapable of providing insights for cell design and evaluation.

To this end, by considering the battery model, mechanical model, phase-field model, and short-circuit model, we establish a physics-based and fully coupled electrochemical-mechanical model for the first time, directly bridging the dendrite growth and crack propagation with battery charging/discharging. After validation of the developed model, the effects of electrochemically generated stress, charging rate, electrolyte properties (including conductivity, Young's modulus, and fracture toughness) are thoroughly investigated while considering interfacial defects to provide insights and guidance on next-generation ASSBs.

## 2 Coupling strategy

To describe the crack propagation- and dendrite growth-induced battery short circuit during charging/discharging in ASSBs, we consider four models: 1) the battery model solves the potential and concentration evolution within the electrode and electrolyte during the charging/discharging process; 2) the mechanical model calculates the deformation, stress, and strain fields caused by the overpotential-driven dendrite growth under the constraint of the SE; 3) the phase-field model is used to describe the crack propagation and dendrite growth; and 4) the short-circuit model detects the triggering of the short circuit and calculates the short-circuit resistance.

To couple the four models described above, the following coupling strategy is adopted (**Figure 1**) with all parameters given (Table 1). During charging, the battery model outputs the overpotential $\eta_-$ to the mechanical model, generating the mechanical stress in the SE.[10c, 16, 19, 24] Then the mechanical model outputs the stress ($\sigma$)-induced strain energy density ($f_{mech}$) to the phase-field model to drive crack propagation. The phase-field model solves the evolution of crack propagation and feeds the phase-field variable $\xi$ ($\xi=1$ for intact/no crack SE, $\xi=-1$ for crack/dendrite) to other models to affect the effective electrolyte conductivity $\sigma_{SE}$ in the battery model, the Young's modulus $E_{SE}$ in the mechanical model, and the short-circuit resistance $R_{short}$ in the short-circuit model. Once $\xi=-1$ (i.e., dendrite) is detected at the cathode/electrolyte interface, the short-circuit model feeds the short-circuit resistance $R_{short}$ to the battery model, causing the voltage drop.

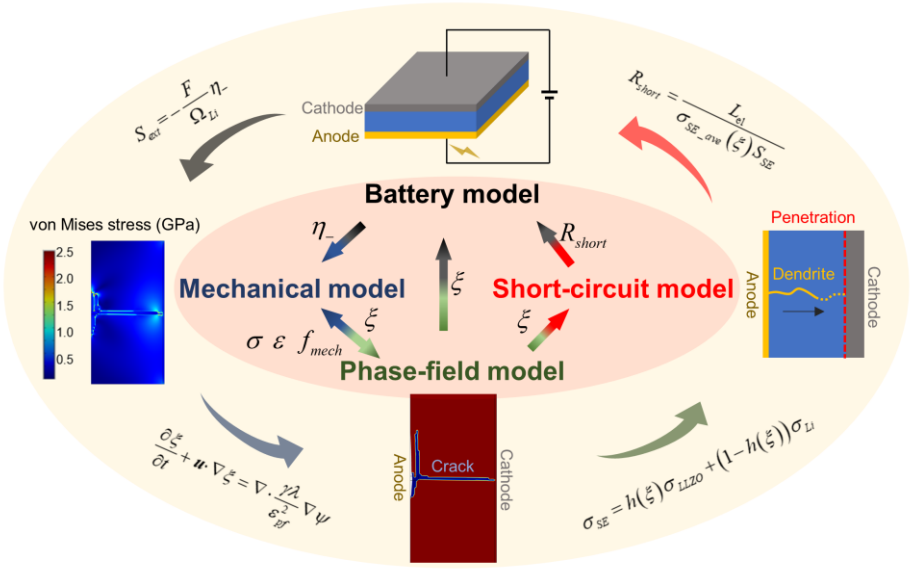


**Figure 1.** Multiphysics coupling strategy for battery model, mechanical model, phase-field model, and short-circuit model.

The promising inorganic solid electrolyte LLZO with high conductivity, high Young's modulus, and wide electrochemical stability window[25] is selected in this study. To generalize the model to accommodate both single-crystal and polycrystalline LLZO and to describe crack propagation/dendrite growth from the cell level, the SE is modeled as a homogenized domain (**Figure 2**), which also facilitates the consideration of battery models. Li metal and $LiCoO_2$(LCO) are used as the anode and cathode, respectively. The left boundary of the electrolyte is considered as the Li anode, according to previous literature,[26] and the right boundary of the cathode is fixed (**Figure 2**). The focus of this study is on the dendrite growth during the charging process without consumption of the Li anode. Then it is assumed that the electrode/electrolyte interfaces have perfect contact and no stacking pressure is applied. The thicknesses of the electrolyte and cathode are $L_{el}$ and $L_{ca}$, respectively, and the battery width is $W_{bat}$. The cell capacity is 1400 μAh/cm$^2$. We designate the pre-defect at the Li/SE interface to represent the unavoidable interfacial defects, such as voids, impurities, and cracks (pre-defects in different dimensions cause similar crack propagation behavior (Figure S1a in the Supporting Information)). The absence of interfacial defect can suppress the dendrite initiation/formation, and makes the battery electrochemical performance better (Figure S1b), which indicates that elimination of the interfacial defect is an effective method for suppression of Li dendrite in solid electrolyte. However, currently, the interfacial defects are inevitable, then the focus of this study is on the influence of interfacial defect. Considering the computational efficiency, the pre-existing defect is rectangular with length $L$=100 μm and width $W$=50 μm. The defect

dimension is much smaller (<10%) than the solid electrolyte, and is at the same magnitude of the crack width reported in the literature.[7b]

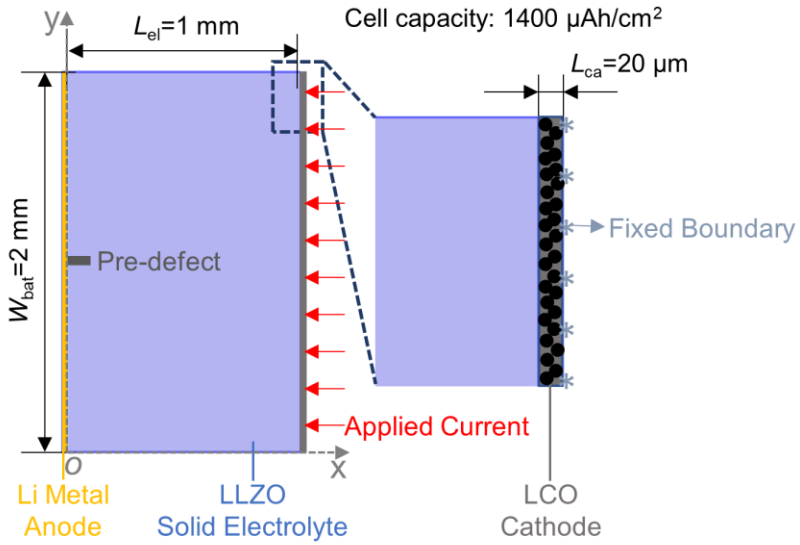


**Figure 2.** Schematics of the established model including geometry, boundary condition, and defect area.

## 3 Results and discussion

### 3.1 Representative results

The charging/discharging voltage versus capacity response of the Li/SE/LCO cell from simulation (Figure S2 in Supporting Information) agrees well with experimental results, and the predicted critical current density is comparable to the reported value, demonstrating the validity of the electrochemical response of the model.

With the pre-existing defect and under a 1C charging rate, the Li dendrite grows around the defect from the beginning of charge until the short circuit. **Figure 3** summarizes the dendrite growth process using the battery model, mechanical model, phase-field model, and short-circuit model. According to the battery model, the battery voltage increases

during the charging process until 423.8 s, at which point the dendrite leads to the short circuit and the voltage drops (**Figure 3**a).

During the charging process, an uneven overpotential $\eta_{-}$ distribution around the pre-existing defect surface affects the interfacial chemical reaction,[16] leading to Li plating around this area (battery model). Since the Li dendrite affects the effective electrolyte conductivity $\sigma_{SE}$ (Equation 6), the electrolyte potential $\phi_l$ changes accordingly (Equation 4) and affects the current density within the SE (**Figure 3**d and Figure S3 in the Supporting Information). The high-conductivity dendrite area further facilitates the Li electrodeposition, i.e., dendrite growth, and accelerates the uneven overpotential $\eta_{-}$ distribution (phase-field model to battery model).

In addition, the uneven overpotential $\eta_{-}$ distribution can change the von Mises stress $\sigma_{\text{Mises}}$ (**Figure 3**c) and cause crack propagation due to the mechanical strain energy density. The cracks initially become large in random directions, then transverse mainly in the direction from the anode side towards the cathode side (**Figure 3**b) (battery model to mechanical model). The cracks provide space for Li dendrite growth (mechanical model to phase-field model). In return, the Li dendrite affects the von Mises stress $\sigma_{\text{Mises}}$ and crack propagation (phase-field model to mechanical model). The strong correlation between the mechanical model and the phase-field model leads to a similar von Mises stress and phase-field distribution within the SE, as shown in **Figures 3**b and c.

However, once the dendrite grows to reach the cathode side, the phase-field variable $\xi = -1$ is detected at the LCO/LLZO interface at $t$=423.8 s, then the direct electron transportation path is built between the anode and cathode and the current density is mainly concentrated within the dendrite area (**Figure 3**d), causing the abrupt voltage drop, i.e., the short circuit (Video 1) (short-circuit model).

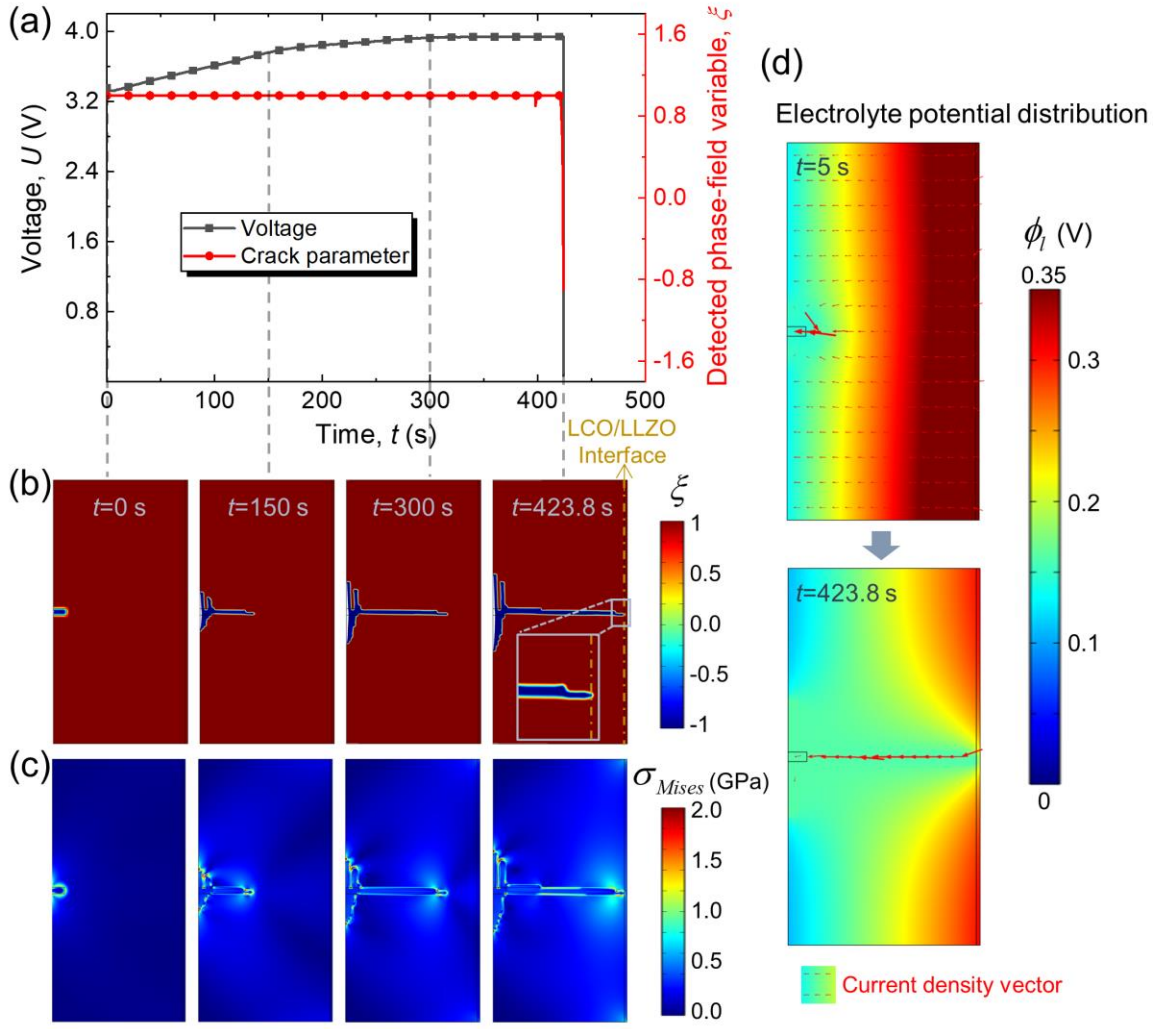


**Figure 3. Representative computational results at 1C charging rate.** (a) voltage response and detected phase-field variable $\xi$ at the LCO/LLZO interface at 1C charging rate; (b) dendrite growth $\xi$ evolution ($\xi = -1$ for dendrite/crack, $\xi = 1$ for intact solid electrolyte); (c) von Mises stress evolution $\sigma_{\text{Mises}}$; (d) electrolyte potential distribution and current density vector (the thicker and longer arrow indicates larger current density) at the beginning and ending time.

In the following discussion, representative simulation results are taken as the baseline, and the parametric study is carried out to understand the governing effects of stress, charging rate, Young's modulus $\sigma_{LLZO}$, and fracture toughness $K_{LLZO}$ on crack propagation/dendrite growth in the SE and the electrochemical response of the battery.

### 3.2 Governing effect from overpotential-driven stress

During the charging process, there inevitably exists the overpotential $\eta_-$ at the Li anode/electrolyte interface. The negative $\eta_-$ will drive Li plating along the SE and the Li interface (**Figure 4**a). Without the stress effect (i.e., Equation 18 is disabled), there is no driving force for crack formation/propagation and dendrite growth, and thus no short circuit occurs. The average SE conductivity is kept constant, and the normal voltage profile during the charging process can be seen in **Figure 4**b. When the overpotential-driven stress is considered, the stress may drive the dendrite growth and crack propagation. As long as the current density exists within the SE, there is a continuous driving force to the newly grown dendrite for further development (**Figure 4**a).

At the beginning of charge (0~150 s), the battery voltage responses are close to each other, with and without taking stress into consideration, indicating Li plating behavior. After that, the discrepancy in voltages gradually appears and amplifies. The baseline voltage is much lower (**Figure 4**b), caused by the conductivity change in the SE as a result of dendrite formation. As the dendrite grows, the effective electrolyte conductivity $\sigma_{SE}$ evolves following the governing law described in Equation 6. Since the electrical

conductivity in the Li dendrite ($\sigma_{Li} = 1.1\times10^{7}$ S/m) is several orders of magnitude higher than the ionic conductivity of the LLZO electrolyte ($\sigma_{LLZO} = 4.43\times10^{-2}$ S/m), the dendrite growth significantly increases the effective electrolyte conductivity (**Figure 4**c). Moreover, $\sigma_{SE}$ significantly influences the current density distribution within the SE because the current density tends to concentrate at the high $\sigma_{SE}$ region (**Figure 4**c), leading to an obvious voltage discrepancy (**Figure 4**b). At *t*=423.8 s, if the stress effect is enabled, the battery voltage abruptly drops, indicating that the Li dendrite finally reaches the cathode side and the short circuit is triggered (Figure S4a in the Supporting Information). It is important to note that the voltage response with dendrite growth obviously deviates from normal battery voltage behavior, which inspires us to propose a possible method for the detection of crack and dendrite issues by monitoring the voltage-time curve for real-time battery health management.

The $\eta_{-}$-driven stress mainly distributes close to the dendrite/electrolyte interface, especially at the dendrite tip (Figure S4b in the Supporting Information). According to Equation 18, the generated stress is linearly related to the overpotential. Under a 1C charging rate, the stress tensor components $\sigma_{ij}\left(i, j = x, y\right)$, and $\sigma_{\text{Mises}}$ all reach the magnitude of GPa (**Figure 4**d). Such large internal stress causes the strain energy density of $10^{8}$ N/m$^{2}$ (Figure S4c in the Supporting Information), providing a sufficient driving force for crack propagation. The continuous and direct propagation of the crack towards the cathode side (i.e., the transverse direction) is responsible for the internal short circuit. In the meantime, the crack propagates laterally as well, along with the anode/electrolyte

interface in the block shape, mainly due to the free mechanical boundary condition for the left boundary and the relatively smaller $\sigma_{xx}$ (Figure S4d in the Supporting Information). Note that the Li dendrite soon fills the crack such that no break-apart of the SE is considered here. The stress at the dendrite tip is more concentrated, including $\sigma_{ij}\left(i, j = x, y\right)$ and $\sigma_{\text{Mises}}$ (**Figure 4**d), and the stress component $\sigma_{yy}$ is larger than $\sigma_{xx}$ (Figure S4d in the Supporting Information), which can elucidate the faster crack propagation speed in the transverse direction than in the lateral direction.

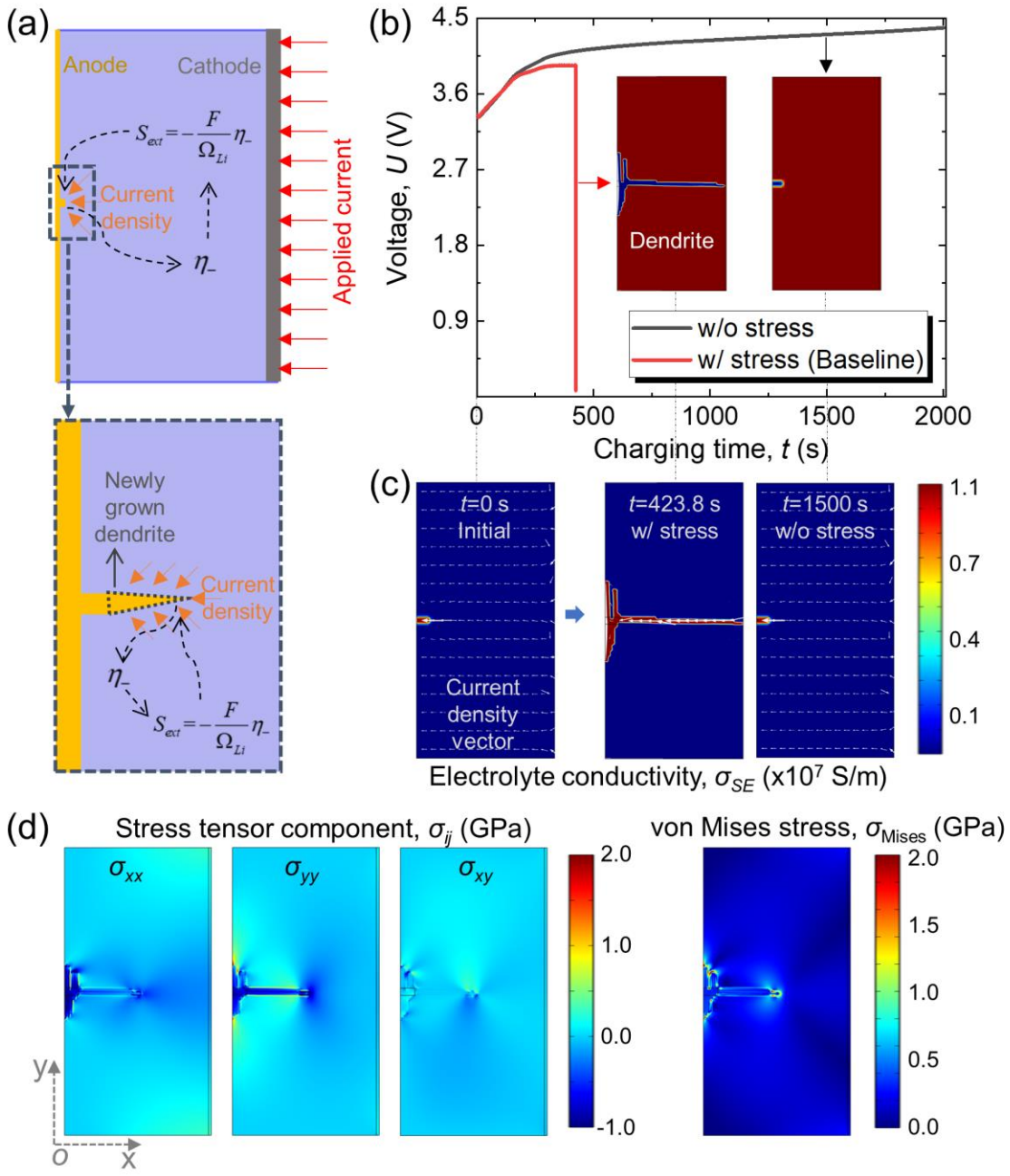


**Figure 4. Effect of electrochemically induced stress at 1C charging rate.** (a) schematics of the crack propagation/dendrite growth driven by the overpotential-induced stress; (b) voltage vs. time curves for models without and with the stress effect; (c) effective electrolyte conductivity $\sigma_{SE}$ and current density vector (the thicker and longer arrow indicates larger current density); (d) stress tensor components $\sigma_{xx}$, $\sigma_{yy}$, $\sigma_{zz}$ and von Mises stress $\sigma_{\text{Mises}}$ at $t$=200 s.

### 3.3 Governing effect from the charging rate

Since the current applied to the battery is determined by the charging rate (C-rate) and the current density within the SE is affected as well to influence the overpotential value, the increased C-rate ultimately results in larger driving stress for faster crack propagation and dendrite growth (**Figure 5**a). Thus, we investigate the C-rate effect on the crack and the electrochemical behavior considering the values of 0.1C, 0.25C, 0.5C, 1C, 1.5C, and 2C (i.e., current density values of 140, 350, 700, 1400, 2100, 2800 μA/cm$^2$, respectively).

The battery overpotentials increase with increasing charging rates. For a C-rate no greater than 0.25C, there is no short circuit during the entire charging process. However, once the C-rate exceeds 0.5C, an abrupt voltage drop (i.e., short circuit) is observed (**Figure 5**b). The higher the charging rate, the less time it takes for a short circuit.

The dendrite growth behavior is also closely related to the C-rate. The Li plating mainly grows along the anode/electrolyte interface (*y*-axis in **Figure 5**c) when the C-rate ≤ 0.25C because the left boundary is free, leading to energy-favorable crack growth. For the C-rate ≥ 0.5C, the dendrite grows transversely (along the *x*-axis) to the cathode in a more slender shape (**Figure 5**c). Moreover, at the short-circuit time, the dendrite grows more in the *y*-axis at higher C-rates, since the stress tensor components $\sigma_{ij}\left(i, j = x, y\right)$ and von Mises stress $\sigma_{\text{Mises}}$ increase with C-rate, and are also large enough under a high C-rate to drive the dendrite propagating in the *y*-axis (Figure S5a in the Supporting Information). The fundamental reason for the larger stress is the larger electrochemical

overpotential $\eta_-$ at a higher C-rate; $\eta_-$ almost remains the same for each C-rate (Figure S5b in the Supporting Information). The distribution of electrolyte potential $\phi_l$ for different C-rates at $t$=200 s (**Figure 5**d) shows that a large C-rate significantly increases the $\phi_l$ at the Li/LLZO interface, i.e., from ~0.04 V under 0.1C to ~0.25 V at 2C, which further validates the large overpotential induced by the high C-rate. Based on $\eta_-$ and the short-circuit time $t_{\text{short}}$, we establish a safety guidance map for dendrite-induced short circuits (**Figure 5**e), where the safety region indicates that no short circuit occurs during the whole charging process if the C-rate<0.25C and $\eta_-$>-0.10 V.

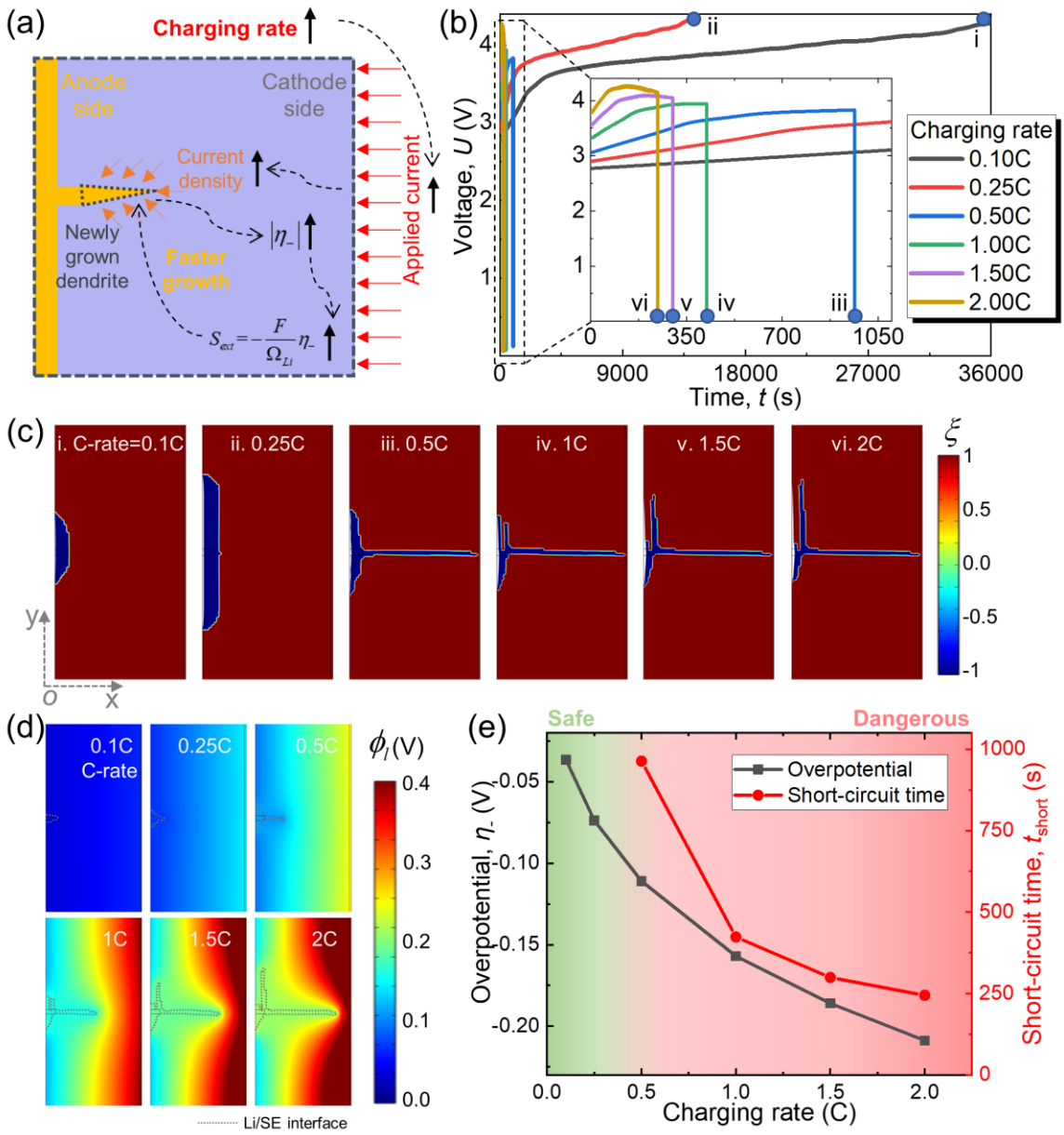


**Figure 5. Effect of charging rate.** (a) schematics of the charging-rate effect on dendrite growth; (b) voltage vs. time curves; (c) contour plots of phase-field parameter $\xi$; (d) electrolyte potential $\phi_l$ distribution at $t$=200 s; (e) safety guidance map based on overpotential $\eta_-$/short-circuit time $t_{\text{short}}$.

### 3.4 Governing effect from the electrolyte conductivity

Improving the electrolyte conductivity is one of the major means of improving the electrochemical behaviors of the ASSB. Here, the LLZO electrolyte conductivity $\sigma_{LLZO}$ effect on the crack and the electrochemical response is explored. Based on the baseline

model, we consider the scenarios of $2.215\times10^{-2}$ S/m, $4.43\times10^{-2}$ S/m, $4.43\times10^{-1}$ S/m, and 4.43 S/m.

Since the electrolyte conductivity directly influences the internal resistance, the electrochemical response of the battery is expected to change. The voltage of the battery during charging is higher under lower $\sigma_{LLZO}$ (**Figure 6**a), because a smaller $\sigma_{LLZO}$ leads to larger battery internal resistance, which indicates that under the same current density (1C is used for all cases here), a higher voltage will be observed. A lower $\sigma_{LLZO}$ corresponds to an earlier short-circuit time, i.e., *t*=374.4 s, 423.8 s, 553.5 s, and 601 s for $\sigma_{LLZO}=2.215\times10^{-2}$ S/m, $4.43\times10^{-2}$ S/m, $4.43\times10^{-1}$ S/m, and 4.43 S/m, respectively (**Figure 6**a). The *x*-axis crack propagation is dominant, and the crack morphology is similar at different $\sigma_{LLZO}$ values (**Figure 6**b). The only slight difference is that there is a slim crack in the *y*-direction under small $\sigma_{LLZO}$ (i.e., $2.215\times10^{-2}$ S/m and $4.43\times10^{-2}$ S/m).

$\sigma_{LLZO}$ mainly influences the electrolyte potential $\phi_l$, which directly determines the overpotential $\eta_-$. Since the electrolyte with smaller $\sigma_{LLZO}$ bears higher voltage, the electrolyte potential $\phi_l$ is larger under the same applied current density, resulting in a higher absolute value of $\eta_-$, i.e., at *t*=360 s, $\eta_-$=-0.17 V, -0.162 V, -0.14 V, and -0.135 V for $\sigma_{LLZO}$ = $2.215\times10^{-2}$ S/m, $4.43\times10^{-2}$ S/m, $4.43\times10^{-1}$ S/m, and 4.43 S/m, respectively (Figure S6a in the Supporting Information). The higher $\eta_-$ drives larger stress; moreover, both the maximum von Mises stress $\sigma_{\text{Mises\_max}}$ and the average von Mises stress $\sigma_{\text{Mises\_ave}}$ increase with decreasing $\sigma_{LLZO}$ (Figure S6b in the Supporting Information), resulting in the correspondingly greater strain energy density. The evolution

of the phase-field parameter $\xi$ is driven by the elastic strain energy (Equation 28-30). Thus, the dendrites grow faster under smaller $\sigma_{LLZO}$. The above discussion demonstrates that increasing the electrolyte conductivity can not only improve the battery electrochemical performance with a reduced internal resistance, but suppress crack propagation as well.

The dendrite preferentially grows laterally in the *y* direction under a low C-rate (<0.5C) and a high $\sigma_{LLZO}$ ($>4.43\times10^{-1}$ S/m) due to the free left boundary and the smaller driving force; thus, no short circuit occurs (Region 1 in **Figures 6**c-d). Increasing the C-rate or decreasing $\sigma_{LLZO}$ both give rise to greater $|\eta_-|$ (absolute value of $\eta_-$), which causes a stronger driving force for the crack and dendrite, resulting in an earlier short circuit (Regions 2-3 in **Figures 6**c-d). An abrupt change of $|\eta_-|$ between Region 2 and Region 3 can be clearly observed in **Figure 6**c. The critical $|\eta_-|$ value at the boundary of Region 2 and Region 3 is about 0.16 V. $|\eta_-|$ is greater than the critical value with C-rate>1 C and $\sigma_{LLZO}<4.43\times10^{-2}$ S/m, corresponding to the earlier short circuit scenarios. From **Figure 6**d, there exists a specific threshold C-rate (namely, critical current density) value under a certain electrolyte conductivity. At 0.25C or below, there is no short circuit for $\sigma_{LLZO}$ from $2.215\times10^{-2}$ S/m to 4.43 S/m. Increasing $\sigma_{LLZO}$ can reduce $|\eta_-|$ and avoid a short circuit for 0.5C, but if the C-rate>0.5C, $|\eta_-|$ is still large (>0.1V) and the dendrite growth-induced short circuit is only delayed but not completely prevented. By contrast, the C-rate is in the dominant position in terms of controlling the $|\eta_-|$ and avoiding a short circuit.

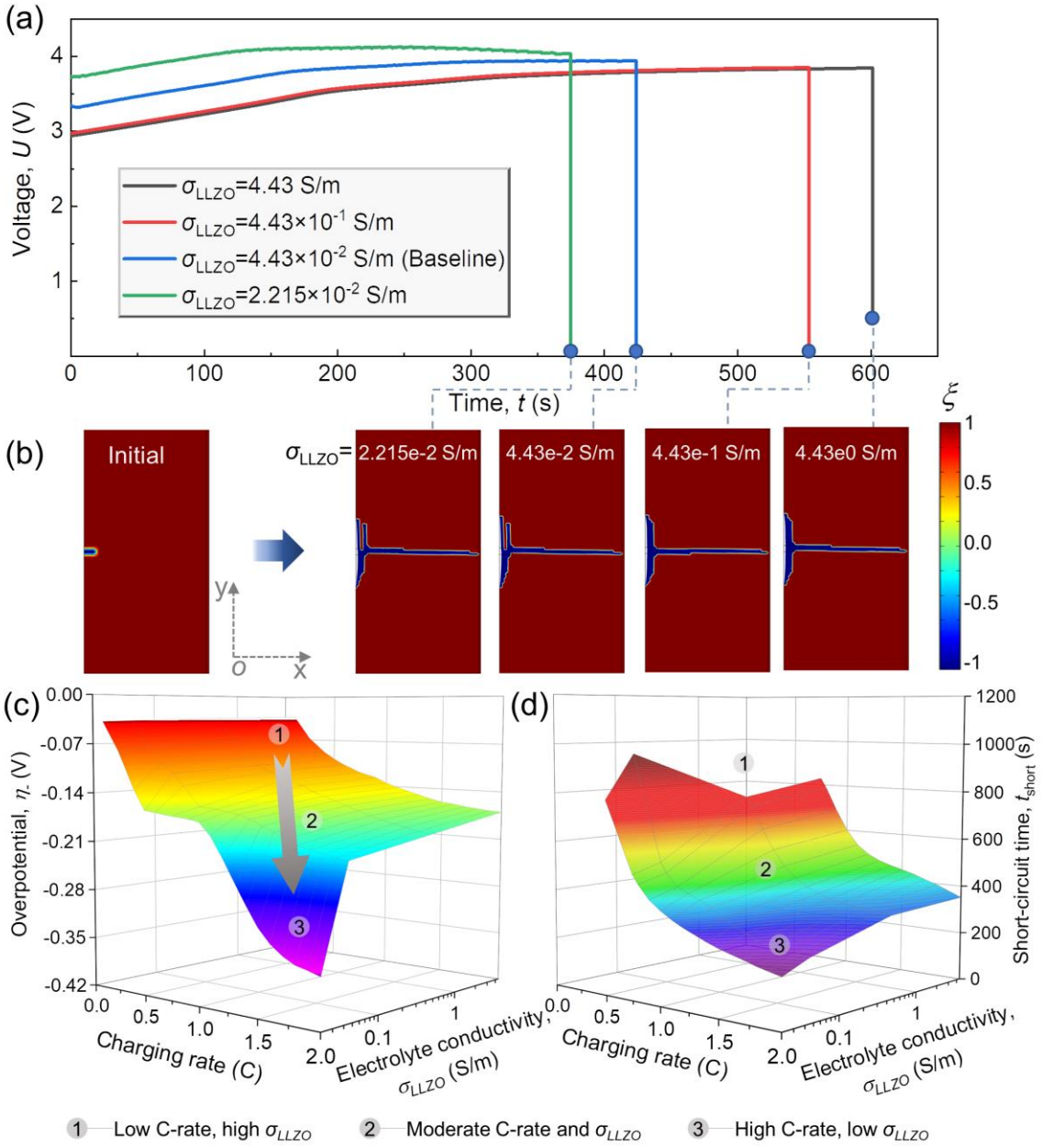


**Figure 6. Effect of electrolyte conductivity**. (a) voltage vs. time curves; (b) contour plots of crack parameter $\xi$ at short-circuit point; coupled effect of charging rate and electrolyte conductivity $\sigma_{LLZO}$ on the (c) overpotential $\eta_-$ and (d) short-circuit time $t_{\text{short}}$.

### 3.5 Governing effect from Young's modulus

In general, a solid electrolyte with a larger Young's modulus is more resistive to deformation. The inherent nature of how an LLZO electrolyte's Young's modulus $E_{LLZO}$ affects the crack propagation and dendrite growth will be investigated here. Based on the baseline model, we select different $E_{LLZO}$, i.e., 15 GPa, 50 GPa, 100 GPa, 150 GPa, and 200 GPa.

According to modeling results, the crack grows only along the Li/LLZO interface for a 15 GPa LLZO SE, shown in **Figure7**a, and no short circuit is observed while the crack growths are along the *x* axis when $E_{LLZO}$ =50 GPa or above. The short circuits are triggered in all these cases, and the short-circuit triggering time $t_{\text{short}}$ decreases with increasing $E_{LLZO}$ if $E_{LLZO}$ <100 GPa, while $t_{\text{short}}$ increases with $E_{LLZO}$ above 100 GPa (**Figure 7**b); $t_{\text{short}}$ is directly related to the transverse dendrite growth. For $E_{LLZO} \geq$100 GPa, the farthest dendrite growth distance *x* is larger for smaller $E_{LLZO}$, while the dendrite growth speed for 50 GPa is much lower when approaching the fixed cathode side (**Figure 7**c), which may explain its longer $t_{\text{short}}$. The low speed at the final stage for 50 GPa is caused by the relatively high fracture energy (**Figure 7**d).

The crack propagation is described from the energy perspective, and $E_{LLZO}$ will significantly influence both the driving force (the elastic strain energy) as well as the fracture threshold energy (the fracture energy *G*) in a competing way. Thus, $E_{LLZO}$ will influence the crack propagation and corresponding dendrite growth as well as the short-

circuit behavior. The maximum/average von Mises stress increases with $E_{LLZO}$ (Figure S7 in the Supporting Information), while the average elastic strain energy density $E_{ave}$ increases with $E_{LLZO} \leqslant 50$ GPa but decreases with increasing $E_{LLZO} > 50$ GPa (**Figure 7**d), which reflects the trends of the driving force. The resistive force $G$ decreases with increasing $E_{LLZO}$ in the whole range (**Figure 7**d). For $E_{LLZO} < 40$ GPa, both the maximum and average strain energy density are much smaller (Figure S7b), and the fracture energy is much higher to resist any crack (**Figure 7**d), demonstrating that $E_{LLZO} < 40$ GPa produces lower driving force and higher resistance for dendrite growth/crack propagation. As a result, the dendrite induced short circuit is delayed or even prevented at the C-rate of 1 C (1400 μA/cm$^2$) with $E_{LLZO} < 40$ GPa, namely the low short-circuit risk, which provides insight for the designing of inorganic solid electrolyte. For 40 GPa$< E_{LLZO} <$100 GPa, $E_{ave}$ maintains at a high level, while $G$ decreases dramatically. Thus, the crack propagates faster, and the short circuit risk is high as well. For $E_{LLZO} > 100$ GPa, both $E_{ave}$ and $G$ decrease, and the short-circuit time is delayed, which is at a medium risk level (**Figure 7**b).

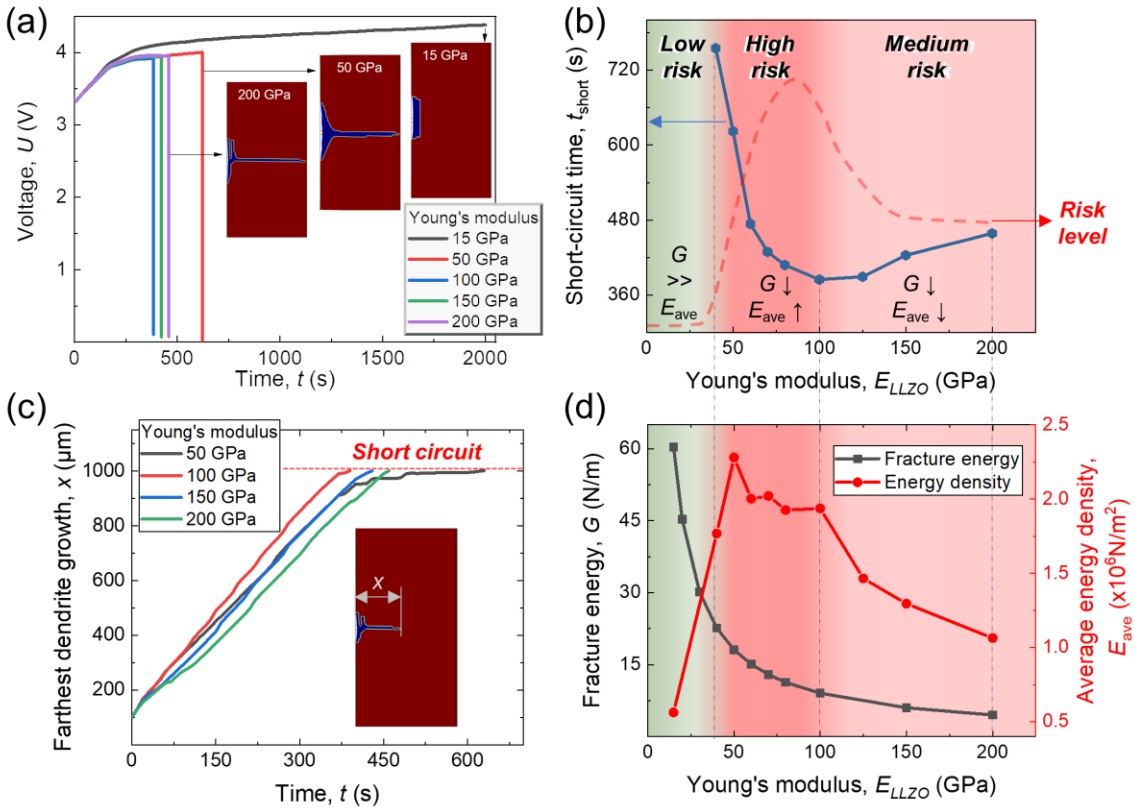


**Figure 7. Effect of Young's modulus**. (a) voltage vs. time curves for different $E_{LLZO}$ ; (b) short-circuit time for different $E_{LLZO}$ ; (c) farthest dendrite growth $x$ in the transverse direction; (d) fracture energy $G$ and average energy density $E_{ave}$ at $t$=250 s as a function of $E_{LLZO}$ .

### 3.6 Governing effect from fracture toughness

The fracture toughness of an LLZO electrolyte $K_{LLZO}$ represents LLZO's capability to resist fracture. Based on the baseline model, different $K_{LLZO}$ values are selected to study the fracture toughness effect, i.e., 0.77, 0.98, 1.24, 1.41, and 1.58 $\text{MPa}\sqrt{\text{m}}$. All other governing factors, i.e., the C-rate (1C), Young's modulus (150 GPa), and pre-defect area, remain the same.

$K_{LLZO}$ only affects the fracture energy. A larger $K_{LLZO}$ represents a higher resistive force to form a crack, resulting in a smaller crack area, which can delay the short-circuit

time. For instance, the short-circuit time increases from $t$=420.3 s to $t$=621.1 s when $K_{LLZO}$ increases from $K_{LLZO} = 0.77\text{MPa}\sqrt{\text{m}}$ to $1.41\text{MPa}\sqrt{\text{m}}$, and may even prevent the short circuit in some extreme cases, e.g., when $K_{LLZO} = 1.58\text{MPa}\sqrt{\text{m}}$ (**Figures 8**a and b). Since the crack propagation speed is faster under smaller $K_{LLZO}$, the dendrite is more prone to penetrate the electrolyte, resulting in an earlier short circuit. Under smaller $K_{LLZO}$, the crack will also propagate laterally ( $K_{LLZO} = 0.77\text{MPa}\sqrt{\text{m}}$ in **Figure 8**b). Straightforwardly, increasing $K_{LLZO}$ can effectively hinder the crack propagation and delay the short-circuit time; if $K_{LLZO}$ is large enough, the crack can even be prevented.

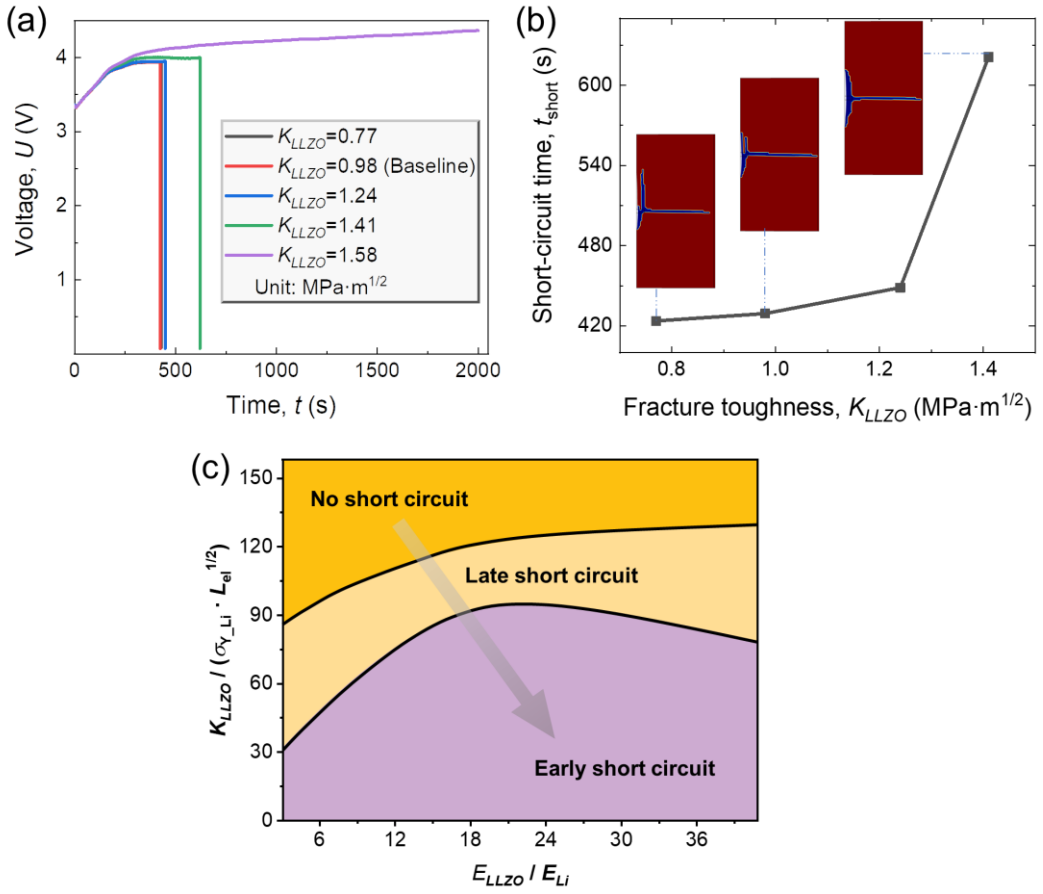


**Figure 8. Effect of fracture toughness**: (a) voltage vs. time curves; (b) short-circuit time $t_{short}$ as a function of fracture toughness $K_{LLZO}$; (c) design map based on the coupled effect of normalized Young's modulus and normalized fracture toughness.

Crack propagation and dendrite growth are responsible for the short circuit. To quantitatively unlock the mechanistic relationship among $E_{LLZO}$, $K_{LLZO}$, and $t$ ($t=\infty$ stands for no short circuit), we establish a mechanism map (**Figure 8**c) with three regions: no short circuit, late short circuit, and early short circuit by using the governing variables of $E_{LLZO}/E_{Li}$ and $K_{LLZO}\Big/\left(\sigma_{Y\_Li}\cdot L_{el}^{\frac{1}{2}}\right)$. The early short circuit covers a large part of the domain, leaving a relatively small portion of the design space. That is why we have witnessed the failure of ASSBs during operation. Generally, larger $K_{LLZO}\Big/\left(\sigma_{Y\_Li}\cdot L_{el}^{\frac{1}{2}}\right)$ leads to higher safety performance, while $E_{LLZO}/E_{Li}$ needs to avoid a certain domain to obtain a larger design space. This straightforward relationship reveals a much boarder design view for the SE in terms of several key mechanical properties with enhanced and optimized safety and cyclability behaviors by mitigating the short-circuit behavior with the desired Young's modulus and fracture toughness.

### 3.7 Implication on engineering application

Plenty of efforts have been attempted to address the scientific and engineering problem: how to realize the applicable all-solid-state battery with appropriate solid electrolyte and at practical current density. The governing effects of stress, charging rate, electrolyte conductivity $\sigma_{LLZO}$, Young's modulus $E_{LLZO}$, and fracture toughness $K_{LLZO}$ have been comprehensively investigated above, which provide the basic guidance for the

development of solid electrolyte and battery management. Based on the findings in this study, we provide insights towards more robust ASSBs in engineering.

The perfect Li/SE interface without any defect has proven to prevent the dendrite initiation and growth (Figure S1b), implying that improvement of Li/SE interfacial property is an effective way to suppress dendrite. However there is inevitable interfacial defect for current inorganic solid electrolyte. One of the main limitations for ASSBs is the critical current density, above which the battery will be short-circuited due to the dendrite growth in solid electrolyte. To make a practical current density for ASSBs, such as 2 $mA/cm^2$ (i.e., 1.5 C in this study, at which dendrite grows to short circuit the battery (**Figure 5**)), both the electrochemical and mechanical properties of the battery can be considered to reduce the driving force and increase the opposing force for dendrite growth/crack propagation. The driving force mainly stems from the overpotential $|\eta_-|$ related strain energy density (lower $|\eta_-|$ corresponds smaller driving force), and the opposing force comes from the fracture energy.

At the practical current density (1.5 C), increasing $\sigma_{LLZO}$ from $2.215\times10^{-2}$ S/m to 4.43 S/m can reduce the $|\eta_-|$ from 0.3 V to 0.16 V, while the reduced $|\eta_-|$=0.16 V is still large enough to cause the dendrite growth- and crack propagation-induced short circuit (**Figure 6**c-d, $t_{short}$ is increased from 263 s to 445 s), which shows that increasing $\sigma_{LLZO}$ can only delay (but not completely inhibit) the occurrence of short circuit at 1.5 C. In addition to improve electrochemical property, the mechanical properties should also be

considered. As indicated in **Figure 7**b, $E_{LLZO}$ below 40 GPa corresponds to the low-risk region with lower strain energy density (driving force) and higher fracture energy (resisting capability), conductive to suppress the dendrite growth. The computational results demonstrate that $E_{LLZO}$ within the low risk region only postpones short circuit at the charging rate of 1.5 C (i.e., $t_{\text{short}}$ is delayed from 445 s at 150 GPa to 674 s at 40 GPa). To completely inhibit the dendrite growth induced short circuit, we need to consider the improvement of $K_{LLZO}$. When $K_{LLZO}$ increases from 0.98 to 1.73 $\text{MPa}\sqrt{\text{m}}$, the dendrite growth is in block shape along *y*-axis rather than the long strip shape in *x*-axis (Figure S8), such that the dendrite induced short circuit is prevented.

Such computation results show a promising direction towards realizing applicable ASSBs with inorganic solid electrolyte after modulation of electrolyte conductivity (~$10^{-1}$ S/m), Young's modulus (<50GPa) and fracture toughness (>1.7 $\text{MPa}\sqrt{\text{m}}$).

## 4 Conclusion

Dendrite growth- and interfacial issues-induced battery failure and poor cyclability are the two main problems hindering the further commercialization of ASSBs. To understand the dendrite growth and crack propagation behavior during battery charging/discharging, considering the interfacial defect, we developed a fully coupled electrochemical-mechanical model, including the battery model, mechanical model, phase-field model, and short-circuit model. After validation, the effects of electrochemically generated stress, charging rate, electrolyte properties (including conductivity, Young's modulus, and fracture

toughness) are comprehensively investigated. When the electrochemically driven stress is considered, there is crack propagation in the SE, and the battery voltage response is different. Eventually, the short circuit is triggered due to dendrite penetration through the SE. We have reached the following conclusions:

- The short circuit occurs earlier with higher C-rate (i.e., C-rate exceeds 0.5C) due to the larger overpotential $|\eta_-|$-driven crack propagation and dendrite growth.
- The overpotential $|\eta_-|$ increases with decreasing electrolyte conductivity, resulting in an earlier short circuit.
- Increasing $\sigma_{LLZO}$ can reduce the internal resistance to improve the battery electrochemical performance, as well as lower the crack propagation speed (delaying the internal short-circuit time).
- The Young's modulus $E_{LLZO}$ affects both the competing mechanism serving as a driving force (strain energy density) and the resistance (fracture energy) for the crack. $E_{LLZO}$ within 40~100 GPa accelerates the crack propagation, causing a high short-circuit risk.
- A larger electrolyte fracture toughness $K_{LLZO}$ can suppress or even stop the crack propagation, significantly reducing the internal short circuit risk.

Note that during the contact between Li dendrite and the pristine SE, our linear elastic description of the Li metal model may over predict the crack propagate slightly (*Supporting Information*) while during the Li dendrite growing stage, such simplification for Li dendrite has no effects on the results. The domains of lithium dendrite and solid electrolyte are

evolving and changing in phase-field methodology, posing great challenges and limitations in defining the complicated mechanical property of the moving area and the interfacial area in the phase field model. In the meantime, the focus of this study is on the interfacial-defect-induced dendrite growth during charging/discharging in cell scale, and the influence of electronic conductivity mainly reflected in micro-scale is not included in the current study. Future work would be considered to solve these limitations.

The established physics-based modeling framework unravels the physics-based mechanisms of the crack propagation, dendrite growth, and electrochemical behavior of the ASSBs during charging/discharging. In the meantime, the mechanism map offers critical guidance for the design, evaluation, and improvement of next-generation robust ASSBs.

## 5 Modeling methodology

***The battery model*** calculates the electrochemical status during charging/discharging, including the evolution of the potential and ion concentration. The inorganic solid electrolyte is a single-ion conductor such that only Li ions migrate within the electrolyte to transport charge. Based on the precondition of electroneutrality, the Li-ion concentration is assumed to be uniform in the solid electrolyte.

Since the anode is pure Li metal and no ohmic loss is considered, the anode domain can be neglected. The left boundary of the electrolyte is the Li/LLZO interface, where the charge-transfer kinetics are governed by the Butler-Volmer equation:[26]

$$j = j_{0-}\left[\exp\left(\frac{\alpha_a F}{RT}\eta_-\right) - \exp\left(\frac{-\alpha_c F}{RT}\eta_-\right)\right] \quad (1)$$

$$j_{0-} = j_{0-,ref}\left(T\right) \quad (2)$$

where $j$ is the current density; $j_{0-}$ is the exchange current density at the anode/electrolyte interface; $\alpha_a$ and $\alpha_c$ are anodic and cathodic charge-transfer coefficients, respectively; $F$ is Faraday's constant, $R$ is the gas constant, $T$=300 K is the temperature; $j_{0-,ref}$ is the reference exchange current density. $\eta_-$ is the overpotential for the electrochemical reaction at the Li/LLZO interface, defined in the following equation:

$$\eta_- = \phi_{s,ext} - \phi_l \quad (3)$$

where $\phi_{s,ext}$ is the external electric potential for the Li anode and $\phi_l$ is the electric potential in the electrolyte phase. Since the anode potential is considered as the ground potential, then $\phi_{s,ext} = 0\text{V}$.

Within the LLZO electrolyte, the electric potential is related to the current density, governed by Ohm's law:

$$\mathbf{i}_l = -\sigma_{SE}\nabla\phi_l \quad (4)$$

where $\mathbf{i}_l$ is the current density in the electrolyte and $\sigma_{SE}$ is the effective conductivity of the electrolyte. Charge conservation requires:

$$\nabla\cdot\mathbf{i}_l = 0 \quad (5)$$

During charging of the battery, the Li dendrite will grow from anode to cathode, which will affect $\sigma_{SE}$:

$$\sigma_{SE} = h\left(\xi\right)\sigma_{LLZO} + \left(1-h\left(\xi\right)\right)\sigma_{Li} \quad (6)$$

where $\xi$ is the phase-field parameter for crack propagation and $\sigma_{LLZO}$ and $\sigma_{Li}$ are the conductivities of LLZO and Li, respectively. The function $h(\xi)=-\frac{1}{4}\xi^3+\frac{3}{4}\xi+\frac{1}{2}$ is used for the interpolation of material properties of the interface between the LLZO electrolyte and the Li dendrite,[27] i.e., conductivity, Young's modulus.

At the electrolyte/cathode interface, the electrochemical reaction kinetics are given by the Butler-Volmer equation as well:

$$j = j_{0+}\left[\exp\left(\frac{\alpha_a F}{RT}\eta_+\right)-\exp\left(\frac{-\alpha_c F}{RT}\eta_+\right)\right] \tag{7}$$

$$j_{0+} = j_{0+,ref}\left(T\right)\left(\frac{c_s}{c_{s,ref}}\right)^{\alpha_c}\left(\frac{c_{s,max}-c_s}{c_{s,max}-c_{s,ref}}\right)^{\alpha_a} \tag{8}$$

where $j_{0+}$ is the exchange current density at the cathode/electrolyte interface; $j_{0+,ref}$ is the reference exchange current density; $c_s$ and $c_{s,ref}$ are the Li-ion concentration and reference Li-ion concentration in the solid phase of the cathode, respectively; and $c_{s,max}$ is the maximum Li-ion concentration. $\eta_+$ is the overpotential for the electrochemical reaction at the LCO/LLZO interface, expressed as:

$$\eta_+ = \phi_s - \phi_l - E_{eq} \tag{9}$$

where $\phi_s$ and $\phi_l$ are the electric potentials in the cathode solid phase and the electrolyte phase, respectively; $E_{eq}$ is the equilibrium potential. $\phi_s$ is given by Ohm's law:

$$\mathbf{i}_s = -\sigma_s \nabla \phi_s \tag{10}$$

where $\mathbf{i}_s$ is the current density in the solid phase of the cathode and $\sigma_s$ is the electrical conductivity of the LCO cathode.

Porous electrode theory is adopted to describe the physicochemical phenomena in cathode domain,[28] which sets up current balance for the porous electrode matrix and the pore electrolyte, as well as the mass balance for the pore electrolyte and for Li ions in the electrode particles. Charge conservation requires:

$$\nabla \cdot \mathbf{i}_s = 0 \tag{11}$$

The ion transport in electrolyte within cathode is neglected, and only ion intercalation in cathode particles is considered based on two assumptions: 1) the inorganic solid electrolyte is single-ion conductor in which only Li ions move to transport charge, 2) conservation of charge is maintained within the solid electrolyte, then the ion concentration in electrolyte is considered constant. Therefore, The electron transport is considered in the whole cathode domain including the electrolyte and particles, governed by the Ohm's law (Equation 4 and 10). The diffusion of Li ions in the active particle of the cathode is governed by Fick's second law:

$$\frac{\partial c_s}{\partial t} = \nabla \cdot \left( D_s \nabla c_s \right) \tag{12}$$

where $D_s$ is the Li-ion intercalation diffusivity.

Based on the above governing equations, the following boundary conditions are applied for the battery model.

$$\frac{\partial c_s}{\partial x} = \frac{-j}{F D_s} \quad \text{at} \quad x = L_{\text{el}} \tag{13}$$

$$\frac{\partial c_s}{\partial x} = 0 \quad \text{at} \quad x = L_{\text{el}} + L_{\text{ca}} \tag{14}$$

$$-\mathbf{i}_s \cdot \mathbf{n} = i_{app} \quad \text{at} \quad x = L_{\text{el}} + L_{\text{ca}} \tag{15}$$

where **n** is the unit outward normal vector of the cathode surface and $i_{app}$ is the applied electrode current density at the right boundary of the cathode.

***The mechanical model*** solves the stress and strain fields when the battery suffers electrochemically driven stress. In this study, only small and elastic deformations are considered, as LLZO has a large Young's modulus (i.e., 150 GPa) with a good capability to resist deformation. The governing equation of the mechanical model follows Newton's second law:

$$\rho \frac{\partial^2 \boldsymbol{u}}{\partial t^2} = \nabla \cdot \boldsymbol{F}_L \left( S + S_{ext} \right) + F_V \tag{16}$$

where $\boldsymbol{u}$ is the displacement field, $\rho$ is the material density, $\boldsymbol{F}_L$ is the deformation gradient, $S$ is the Piola-Kirchhoff stress tensor, $S_{ext}$ is the external stress tensor representing the load contribution from electrochemical overpotential-driven stress, and $F_V$ is the body force. The deformation gradient can be expressed as:

$$\boldsymbol{F}_L = \boldsymbol{I} + \nabla \boldsymbol{u} \tag{17}$$

where $\boldsymbol{I}$ is the identity matrix and $\boldsymbol{u}$ is the displacement vector.

The overpotential at the interface of the Li dendrite and the electrolyte $\eta_{\_}$ drives the dendrite growth under the constraint of the SE, determining the value of hydrostatic stress (i.e., the external stress tensor). For other regions except for the dendrite/electrolyte interface, there is no overpotential influence on the hydrostatic stress. Then, the relationship between $S_{ext}$ and $\eta_{\_}$ can be expressed as:[16, 19, 29]

$$S_{ext}=\begin{cases}-\dfrac{F}{\Omega_{Li}}\eta_{-} & \text{at dendrite/electrolyte interface}\\ 0 & \text{for other region}\end{cases} \tag{18}$$

where $\Omega_{Li}$ is the partial molar volume of Li metal.

As the crack propagates and the dendrite grows, the Young's modulus of the solid electrolyte $E_{SE}$ evolves as well, represented as:

$$E_{SE}=h(\xi)E_{LLZO}+(1-h(\xi))E_{Li} \tag{19}$$

where $E_{LLZO}$ and $E_{Li}$ are Young's moduli of the LLZO electrolyte and the Li dendrite, respectively.

As for the mechanical boundary conditions, the right boundary of the cathode is fixed:

$$u_x=u_y=0 \quad \text{at} \quad x=L_{\text{el}}+L_{\text{ca}} \tag{20}$$

The crack propagation is described by the evolution of the non-conserved phase-field order parameter $\xi$ of the ***phase-field model*** in this study from the perspective of energy. $\xi=1$ and $\xi=-1$ represent the intact electrolyte region and the cracked region, respectively. The phase-field method uses a diffuse interface to show the continuous phase-field variable across the interfacial region, and $-1<\xi<1$ is the transition interface between the intact and cracked regions. Note that it is assumed that the cracked region is filled with Li dendrite.[8b, 20a, 30] The total free energy of the system in this study is expressed as follows:[8b, 27, 31]

$$F_{total}=\int\left[f_{local}+f_{grad}+f_{mech}\right]\mathrm{d}V \tag{21}$$

where $f_{local}$ is the local energy density, $f_{grad}$ is the gradient energy density, and $f_{mech}$ is the mechanical strain energy density, whose expressions are written as:

$$f_{local} = \frac{\lambda}{4\varepsilon_{pf}^2}(1-\xi)^2(1+\xi)^2 \tag{22}$$

$$f_{grad} = \frac{\lambda}{2}(\nabla\xi)^2 \tag{23}$$

$$f_{mech} = \frac{1}{2}\sigma_{ij}\varepsilon_{ij} = \frac{1}{2}C_{ijkm}(\xi)\varepsilon_{ij}\varepsilon_{km} \tag{24}$$

where $\lambda$ is the mixing energy density, $\varepsilon_{pf}$ is the parameter controlling the interface thickness, $C_{ijkm}(\xi)$ is the stiffness (i.e., Young's modulus $E_{SE}$ in Equation 19), and $\varepsilon_{km}$ are strain components. The relationship between $\lambda$ and $\varepsilon_{pf}$ follows:[31]

$$\lambda = \frac{3E_\sigma\varepsilon_{pf}}{\sqrt{8}} \tag{25}$$

where $E_\sigma$ is the surface energy required to create the new cracked surfaces. We assume that all the mechanical elastic strain energy is used to drive the crack propagation and is transferred to the surface energy without loss. Due to the fact that each newly formed crack has two identical surfaces, the surface energy $E_\sigma$ is equal to half of the fracture energy $G$:

$$E_\sigma = \frac{G}{2} \tag{26}$$

$$G = \frac{(1-\nu^2)K_{LLZO}^2}{E_{LLZO}} \tag{27}$$

where $K_{LLZO}$ is the fracture toughness of the LLZO electrolyte and $\nu$ is LLZO's Poisson's ratio.

The governing equation for the crack propagation follows the Allen-Cahn equation as:[27]

$$\frac{\partial \xi}{\partial t} + \boldsymbol{u} \cdot \nabla \xi = \nabla \cdot \frac{\gamma \lambda}{\varepsilon_{pf}^2} \nabla \psi \tag{28}$$

where $\gamma$ is the mobility parameter controlling the crack propagation, written as:

$$\gamma = \chi \varepsilon_{pf}^2 \tag{29}$$

where $\chi$ is the mobility tuning parameter reflecting the crack propagation speed. $\psi$ is obtained from the total free energy through the variational method, expressed as:

$$\psi = -\nabla \cdot \varepsilon_{pf}^2 \nabla \xi + \left(\xi^2 - 1\right)\xi + \frac{\varepsilon_{pf}^2}{\lambda} \frac{\partial f_{mech}}{\partial \xi} \tag{30}$$

Since the pre-defect is designated at the Li/LLZO interface, the initial value for the pre-defect region is $\xi = -1$; for the remaining intact regions, the initial value is $\xi = 1$.

Once the crack continuously propagates and the dendrite grows to reach the cathode side, the Li anode and LCO cathode are internally connected by the dendrite, indicating a triggered short circuit.

***The short-circuit model*** is developed to probe whether the dendrite penetrates through the solid electrolyte (i.e., whether $\xi = -1$ at the cathode/electrolyte interface). If the short circuit is detected, the short-circuit resistance $R_{short}$ is calculated by the following equation:

$$R_{short} = \frac{L_{\mathrm{el}}}{\sigma_{SE\_ave}\left(\xi\right) S_{SE}} \tag{31}$$

where $\sigma_{SE\_ave}\left(\xi\right)$ is the average conductivity of the solid electrolyte automatically obtained from the domain probe and $S_{SE}$ is the cross-section area of the electrolyte.

**Table 1.** Summary of material properties and simulation parameters

| Parameter | Symbol | Value | References |
|---|---|---|---|
| Anodic charge transfer coefficients | $\alpha_a$ | 0.5 | [26, 32] |
| Cathodic charge transfer coefficients | $\alpha_c$ | 0.5 | [26, 32] |
| Conductivity of LLZO | $\sigma_{LLZO}$ | $4.43\times10^{-2}$ S/m | [8b, 12b] |
| Conductivity of Li | $\sigma_{Li}$ | $1.1\times10^{7}$ S/m | [8b, 33] |
| Conductivity of LCO cathode | $\sigma_s$ | $1.13\times10^{-1}$ S/m | [34] |
| Li-ion intercalation diffusivity of cathode | $D_s$ | $5\times10^{-13}$ $m^2/s$ | [35] |
| Faraday's constant | $F$ | 96485 C/mol | [8b, 33] |
| Gas constant | $R$ | 8.314 J/mol/K | [8b, 33] |
| Temperature | $T$ | 300 K | [33] |
| Density of LLZO | $\rho_{SE}$ | 4606 $kg/m^3$ | [8b] |
| Density of Li metal | $\rho_{Li}$ | 534 $kg/m^3$ | [8b] |
| Partial molar volume of Li metal | $\Omega_{Li}$ | $1.3\times10^{-5}$ $m^3/mol$ | [8b, 33] |
| Young's modulus of Li metal | $E_{Li}$ | 4.9 GPa | [8b, 22] |
| Young's modulus of LLZO | $E_{LLZO}$ | 150 GPa | [8b, 22] |
| Poisson's ratio of LLZO | $v_{LLZO}$ | 0.257 | [8b, 22] |
| Parameter controlling interface thickness | $\varepsilon_{pf}$ | $1\times10^{-6}$ m | estimated |
| Fracture toughness of LLZO | $K_{LLZO}$ | 0.98 $MPa\sqrt{m}$ | [3a] |
| Mobility tuning parameter | $\chi$ | $6\times10^{-6}$ $(m\cdot s)/kg$ | estimated |

| | | | |
|---|---|---|---|
| Cross-section area of the electrolyte | $S_{SE}$ | 1 $m^2$ | calculated |
| Yield stress of Li metal | $\sigma_{Y\_Li}$ | 0.4 MPa | [23] |

## Declaration of Interests

The authors declare no competing interests.

## Author contribution

**Chunhao Yuan**: Methodology; modeling, and writing – original draft; **Wenquan Lu**: Data analysis and writing – review and editing; **Jun Xu**: Conceptualization, supervision, methodology, and writing – review and editing, review, and editing.

## Data availability

The datasets used in this study are available from the corresponding author upon request.

## Acknowledgments

J.X. and W. Lu greatly appreciated the financial support from the U.S. Department of Energy's Office of Energy Efficiency and Renewable Energy (EERE) under the Advanced Manufacturing Office, award number DE-EE0009111.

## References

[1] a) B. Liu, Y. Jia, C. Yuan, L. Wang, X. Gao, S. Yin, J. Xu, *Energy Storage Mater.* **2020**, 24, 85; b) C. Yuan, L. Wang, S. Yin, J. Xu, *J. Power Sources* **2020**, 467; c) Y. Jia, J. Li, C. Yuan, X. Gao, W. Yao, M. Lee, J. Xu, *Adv. Energy Mater.* **2021**, 11, 2003868.

[2] a) J. Deng, C. Bae, A. Denlinger, T. Miller, *Joule* **2020**, 4, 511; b) H. Wang, Y. Liu, Y. Li, Y. Cui, *Electrochem. Energ. Rev.* **2019**, 2, 509.

[3] a) F. Zhang, Q.-A. Huang, Z. Tang, A. Li, Q. Shao, L. Zhang, X. Li, J. Zhang, *Nano Energy* **2020**, 70; b) W. Zhao, J. Yi, P. He, H. Zhou, *Electrochem. Energ. Rev.* **2019**, 2, 574.

[4] D. Cao, X. Sun, Q. Li, A. Natan, P. Xiang, H. Zhu, *Matter* **2020**, 3, 57.

[5] a) W. Lan, H. Fan, V. W.-h. Lau, J. Zhang, J. Zhang, R. Zhao, H. Chen, *Sustain. Energy Fuels* **2020**, 4, 1812; b) L. Zhang, K. Yang, J. Mi, L. Lu, L. Zhao, L. Wang, Y. Li, H. Zeng, *Adv. Energy Mater.* **2015**, 5.

[6] a) Z. Tong, S. B. Wang, Y. K. Liao, S. F. Hu, R. S. Liu, *ACS Appl. Mater. Inter.* **2020**, 12, 47181; b) Y. Tang, L. Zhang, J. Chen, H. Sun, T. Yang, Q. Liu, Q. Huang, T. Zhu, J. Huang, *Energy Environ. Sci.* **2021**, DOI: 10.1039/d0ee02525a; c) T. Shi, Y.-Q. Zhang, Q. Tu, Y. Wang, M. C. Scott, G. Ceder, *J. Mater. Chem. A* **2020**, 8, 17399; d) D. Wang, C. Zhu, Y. Fu, X. Sun, Y. Yang, *Adv. Energy Mater.* **2020**, 10, 2001318.

[7] a) Z. Ning, D. S. Jolly, G. Li, R. De Meyere, S. D. Pu, Y. Chen, J. Kasemchainan, J. Ihli, C. Gong, B. Liu, D. L. R. Melvin, A. Bonnin, O. Magdysyuk, P. Adamson, G. O. Hartley, C. W. Monroe, T. J. Marrow, P. G. Bruce, *Nat. Mater.* **2021**, DOI: 10.1038/s41563-021-00967-8; b) S. Hao, S. R. Daemi, T. M. M. Heenan, W. Du, C. Tan, M. Storm, C. Rau, D. J. L. Brett, P. R. Shearing, *Nano Energy* **2021**, 82.

[8] a) K. Tantratian, H. Yan, K. Ellwood, E. T. Harrison, L. Chen, *Adv. Energy Mater.* **2021**, 11; b) C. Yuan, X. Gao, Y. Jia, W. Zhang, Q. Wu, J. Xu, *Nano Energy* **2021**, 86.

[9] E. Kazyak, R. Garcia-Mendez, W. S. LePage, A. Sharafi, A. L. Davis, A. J. Sanchez, K.-H. Chen, C. Haslam, J. Sakamoto, N. P. Dasgupta, *Matter* **2020**, 2, 1025.

[10] a) X. Wang, W. Zeng, L. Hong, W. Xu, H. Yang, F. Wang, H. Duan, M. Tang, H. Jiang, *Nat. Energy* **2018**, 3, 227; b) J. Park, D. Kim, W. A. Appiah, J. Song, K. T. Bae, K. T. Lee, J. Oh, J. Y. Kim, Y.-G. Lee, M.-H. Ryou, Y. M. Lee, *Energy Storage Mater.* **2019**, 19, 124; c) Y. Chen, Z. Wang, X. Li, X. Yao, C. Wang, Y. Li, W. Xue, D. Yu, S. Y. Kim, F. Yang, A. Kushima, G. Zhang, H. Huang, N. Wu, Y. W. Mai, J. B. Goodenough, J. Li, *Nature* **2020**, 578, 251.

[11] a) C. L. Tsai, V. Roddatis, C. V. Chandran, Q. Ma, S. Uhlenbruck, M. Bram, P. Heitjans, O. Guillon, *ACS Appl. Mater. Inter.* **2016**, 8, 10617; b) K. K. Fu, Y. Gong, B. Liu, Y. Zhu, S. Xu, Y. Yao, W. Luo, C. Wang, S. D. Lacey, J. Dai, Y. Chen, Y. Mo, E. Wachsman, L. Hu, *Sci. Adv.* **2017**, 3; c) Y. Yin, C.-S. Jiang, H. Guthrey, C. Xiao, N. Seitzman, C. Ban, M. Al-Jassim, *J. Electrochem. Soc.* **2020**, 167.

[12] a) R. Hongahally Basappa, T. Ito, T. Morimura, R. Bekarevich, K. Mitsuishi, H. Yamada, *J. Power Sources* **2017**, 363, 145; b) H.-Y. Li, B. Huang, Z. Huang, C.-A. Wang, *Ceram. Int.* **2019**, 45, 18115.

[13] a) Q. Tu, L. Barroso-Luque, T. Shi, G. Ceder, *Cell Rep. Phys. Sci.* **2020**, 1; b) J. M. Doux, H. Nguyen, D. H. S. Tan, A. Banerjee, X. Wang, E. A. Wu, C. Jo, H. Yang, Y. S. Meng, *Adv. Energy Mater.* **2019**, 10; c) M. J. Wang, R. Choudhury, J. Sakamoto, *Joule* **2019**, 3, 2165.

[14] Y. Qi, C. Ban, S. J. Harris, *Joule* **2020**, 4, 2599.

[15] F. Flatscher, M. Philipp, S. Ganschow, H. M. R. Wilkening, D. Rettenwander, *J. Mater. Chem. A* **2020**, 8, 15782.

[16] L. Porz, T. Swamy, B. W. Sheldon, D. Rettenwander, T. Frömling, H. L. Thaman, S. Berendts, R. Uecker, W. C. Carter, Y.-M. Chiang, *Adv. Energy Mater.* **2017**, 7.

[17] M. Nagao, A. Hayashi, M. Tatsumisago, T. Kanetsuku, T. Tsuda, S. Kuwabata, *Phys Chem Chem Phys* **2013**, 15, 18600.

[18] E. J. Cheng, A. Sharafi, J. Sakamoto, *Electrochim. Acta* **2017**, 223, 85.

[19] L. Zhang, T. Yang, C. Du, Q. Liu, Y. Tang, J. Zhao, B. Wang, T. Chen, Y. Sun, P. Jia, H. Li, L. Geng, J. Chen, H. Ye, Z. Wang, Y. Li, H. Sun, X. Li, Q. Dai, Y. Tang, Q. Peng, T. Shen, S. Zhang, T. Zhu, J. Huang, *Nat Nanotechnol* **2020**, 15, 94.

[20] a) S. S. Shishvan, N. A. Fleck, R. M. McMeeking, V. S. Deshpande, *J. Power Sources* **2020**, 456; b) S. S. Shishvan, N. A. Fleck, R. M. McMeeking, V. S. Deshpande, *Acta Mater.* **2020**, 196, 444.

[21] X. Song, Y. Lu, F. Wang, X. Zhao, H. Chen, *J. Power Sources* **2020**, 452.

[22] H.-K. Tian, Z. Liu, Y. Ji, L.-Q. Chen, Y. Qi, *Chem. Mater.* **2019**, 31, 7351.

[23] A. Verma, H. Kawakami, H. Wada, A. Hirowatari, N. Ikeda, Y. Mizuno, T. Kotaka, K. Aotani, Y. Tabuchi, P. P. Mukherjee, *Cell Rep. Phys. Sci.* **2021**, 2.

[24] R. D. Armstrong, T. Dickinson, J. Turner, *Electrochim. Acta* **1974**, 19, 187.

[25] L. Buannic, B. Orayech, J.-M. López Del Amo, J. Carrasco, N. A. Katcho, F. Aguesse, W. Manalastas, W. Zhang, J. Kilner, A. Llordés, *Chem. Mater.* **2017**, 29, 1769.

[26] S. D. Fabre, D. Guy-Bouyssou, P. Bouillon, F. Le Cras, C. Delacourt, *J. Electrochem. Soc.* **2011**, 159, A104.

[27] B. Liu, J. Xu, *ACS Appl. Energy Mater.* **2020**, 3, 10931.

[28] Marc Doyle, Thomas F. Fuller, J. Newman, *J. Electrochem. Soc.* **1993**, 140.

[29] A. Mistry, P. P. Mukherjee, *J. Electrochem. Soc.* **2020**, 167.

[30] M. Klinsmann, F. E. Hildebrand, M. Ganser, R. M. McMeeking, *J. Power Sources* **2019**, 442.

[31] Y. Hou, P. Yue, Q. Xin, T. Pauli, W. Sun, L. Wang, *Road Mater. Pavement Des.* **2013**, 15, 167.

[32] L. Chen, H. W. Zhang, L. Y. Liang, Z. Liu, Y. Qi, P. Lu, J. Chen, L.-Q. Chen, *J. Power Sources* **2015**, 300, 376.

[33] P. Barai, K. Higa, A. T. Ngo, L. A. Curtiss, V. Srinivasan, *J. Electrochem. Soc.* **2019**, 166, A1752.

[34] M. Tang, P. Albertus, J. Newman, *J. Electrochem. Soc.* **2009**, 156.

[35] D. E. Stephenson, E. M. Hartman, J. N. Harb, D. R. Wheeler, *J. Electrochem. Soc.* **2007**, 154, A1146.